

Article

Spectroscopic Microtomography in the Short-Wave Infrared Wavelength Range

Cory Juntunen ¹, Andrew R. Abramczyk ¹, Peter Shea ¹ and Yongjin Sung ^{1,*}

- College of Engineering and Applied Science, University of Wisconsin-Milwaukee, 3200 N Cramer St, Milwaukee, WI 53211, USA
- * Correspondence: ysung4@uwm.edu
- Abstract: Spectroscopic microtomography provides the ability to perform 4D (3D structural and
- ² 1D chemical) imaging of a thick microscopic specimen. Here we demonstrate spectroscopic micro-
- tomography in the short-wave infrared (SWIR) wavelength using digital holographic tomography,
- 4 which captures both the absorption coefficient and refractive index. A broadband laser in tandem
- with a tunable optical filter allows us to scan the wavelength from 1100 nm to 1650 nm. Using
- $_{\rm 6}$ $\,$ the developed system, we measure human hair and sea urchin embryo samples. The resolution
- estimated with gold nanoparticles is $1.51 \, \mu m$ (transverse) and $1.57 \, \mu m$ (axial) for the field of view of
- $307 \times 246 \,\mu\text{m}^2$. The developed technique will enable accurate and efficient analyses of microscopic specimens that have a distinctive absorption or refractive index contrast in the SWIR range.
- **Keywords:** near-infrared imaging; optical tomography; spectroscopy

1. Introduction

12

14

31

Spectroscopic microtomography records the absorption spectrum (i.e., the absorption coefficient as a function of the wavelength of the interrogating light) at every voxel in the three-dimensional (3D) volume of a microscopic specimen. It has been demonstrated in the visible [1,2], the mid-infrared (MIR) [3,4], and the soft X-ray ranges [5,6], showcasing the value of the information contained within the 4D (3D volume and 1D spectrum) data cube of a wide range of samples. In this paper, we demonstrate spectroscopic microtomography in the short-wave infrared (SWIR) range of 1100-1650 nm, which is the near-infrared (NIR) range where InGaAs cameras produce high sensitivity. Vibrational spectroscopy using infrared absorption or Raman scattering has long been explored as a non-invasive chemical analysis tool as it can provide the molecular fingerprints of a variety of materials and chemical compounds[7]. In comparison with MIR[8] or Raman[9] spectroscopy, NIR spectroscopy in the wavelength range of 800–2500 nm offers different opportunities for chemical imaging[10]. Using overtones and combination bands, the NIR spectrum is not as specific as the MIR or Raman spectra; however, NIR light penetrates more deeply, and therefore can be used to image thicker specimens. Many materials of practical interest have a distinct NIR spectrum, which, in combination with a proper chemometric analysis, allows for accurate classification and regression at much lower time and cost than MIR or Raman spectroscopy. Microscopic imaging using NIR can provide a high resolution with minimal sample preparation and without concern about sample heating[10]. In addition, using NIR, thick biological samples can be imaged in the culture medium in their most native condition, whereas MIR would require compression or dehydration of thick samples.

There are several strategies for spectroscopic microtomography which allow for the 3D spatial reconstruction of a sample while also providing the spectrum at each voxel in the 3D space, resulting in a 4D data cube. Our approach utilizes digital holographic tomography (DHT) and a wavelength scanning light source via a broadband white-light laser and tunable filter, as well as a variable optical path length (VOPL)

Citation: Juntunen, C.; Abramczyk, A.R.; Shea, P.; Sung, Y. Spectroscopic microtomography in the short-wave infrared wavelength range. *Sensors* **2021**, *1*, 0. https://doi.org/

Received: Accepted:

Published:

Publisher's Note: MDPI stays neutral with regard to jurisdictional claims in published maps and institutional affiliations.

Copyright: © 2023 by the authors. Submitted to *Sensors* for possible open access publication under the terms and conditions of the Creative Commons Attribution (CC BY) license (https://creativecommons.org/licenses/by/4.0/).

strategy. DHT can provide the 3D maps of absorption and refractive index by recording both the amplitude and phase images for varying orientations of the sample with respect to the illumination beam. The relative orientation of the sample can be varied 41 by rotating the sample around an axis orthogonal to the optical axis[11], rotating the illumination beam[12,13], or both[14,15]. We use beam-rotation tomography, which is much faster than sample-rotation tomography but suffers more from the missing-cone artefact due to the insufficient angular coverage of the incident beam. DHT is also called 45 tomographic phase microscopy[13], tomographic diffractive microscopy[16], etc. We use a continuum laser with a tunable bandpass filter, which allows for spectroscopic 47 interrogation at selected wavelengths bypassing the lengthy interferogram collection process of Fourier-transform spectroscopy (FTS). FTS can provide a high spectral resolu-49 tion, but it requires the collection of the entire interferogram, which typically consists of 50 more than 1000 samples. Using DHT in combination with a wavelength-scanning laser, 51 we previously demonstrated spectroscopic microtomography in the visible wavelength 52 range, measuring the absorption spectra of oxygenated and deoxygenated blood cells[1]. In this work, we have constructed a new system for spectroscopic microtomography 54 in the SWIR range. Using the developed system, we measure the refractive index and absorption spectrum of a human hair for the wavelength range of 1100 nm to 1650 nm. 56 Although the maximum numerical aperture of the NIR objective lenses was only 0.65, which allowed us to change the illumination angle only up to 40°, we still were able to 58 perform 3D imaging of a human hair and sea urchin embryo. Using gold nanoparticles, we evaluate the 3D imaging performance of the developed system. The demonstrated method opens a new door to chemical imaging of complex microscopic specimens that show absorption contrast in the SWIR range.

2. Materials and Methods

4 2.1. System design

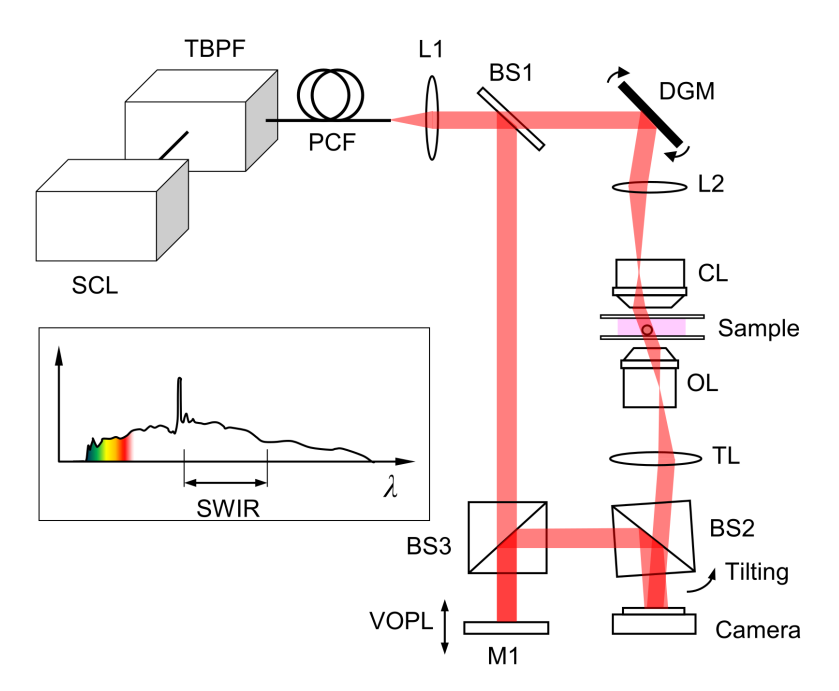


Figure 1. Schematic diagram of the 4D NIR spectral-microtomographic system. As the source light enters the optical system, the sample and reference beam paths are split and combined before images are acquired. SCL: supercontinuum laser; TBPF: tunable bandpass filter; PCF: photonic crystal fiber; L1 and L2: lenses; M1: mirror; BS1, BS2 and BS3: beam splitters; DGM: dual-axis galvanometer mirror; CL: condenser lens; OL: objective lens; TL: tube lens; VOPL: variable optical path length.

Our 4D SWIR system was built in the lab starting with the supercontinuum laser light source (SCL) (NKT Photonics, WL SC400-4) which generates broadband white-light. This white light passes through a tunable bandpass filter (TBPF) (NKT Photonics, SWIR HP8), allowing a spectral band of light narrower than 5 nm (FWHM) to pass through, which is controlled by LabVIEW code. A SuperK Connect broadband fiber coupling unit couples the light to a photonic crystal fiber (PCF), which connects to a cage mount on our optical system. After the PCF, the beam passes through an achromat (L1) with 71 focal length of 100 mm, and an iris for alignment purposes. The beam passes through a 72 beam splitter (BS1) which splits the beam into a sample beam path and reference beam path. The sample beam rotates with dual galvanometer mirrors (DGM) (Cambridge Technology, 8310KM60) to change the angle of incidence of the beam up to 40° with respect to the optical axis. These galvanometer mirrors are controlled by a NI controller and LabVIEW code. After the galvanometer mirrors, the beam passes through the condenser lens (CL) (Mitutoyo, 50x, 0.65 NA) and through the sample which is placed in an appropriate index matching oil and sandwiched between two cover glasses. Next the beam passes through the objective lens (OL) (Mitutoyo, 50x, 0.65 NA) and tube lens (TL) with focal length of 100 mm. Two additional lenses with focal lengths 75 mm and 125 mm (not shown in Fig. 1) are installed before combining with the reference beam. All the lenses in the sample beam path are installed in the 4-f telecentric configuration. For the reference beam, the beam passes through a beam splitter (BS3) and reflects off of a mirror (M1). Mirror M1 is placed on a motorized stage (Thorlabs, MTS50-Z8) which is used to adjust the variable optical path length (VOPL) of the reference beam. Finally, the reference beam passes through another beam splitter (BS2) where the reference beam is combined with the sample beam, producing interference fringes. BS2 is rotated slightly so that the interference between the sample and reference beams produces vertical fringes as opposed to the bullseye pattern fringes. An InGaAs camera (Raptor Photonics, OWL 1.7-VS-CL-1280) composed of 1280×1024 pixels of $10 \, \mu m$ is used to record the raw interferogram images. The overall magnification factor is 41.7, which corresponds to the field of view of $307 \times 246 \,\mu\text{m}^2$, and the pixel resolution is $0.24 \,\mu\text{m}$. The off-axis DHT reduces the resolution by a factor of 3, and the Nyquist criterion further reduces the effective resolution by another factor of 2. Thus, the theoretical resolution of the current design is about 1.44 µm. All optical elements used within the system utilize anti-reflective "C" coating which is optimized for the wavelengths scanned in this demonstration. An additional white-light LED source and a charge-coupled-device (CCD) camera (Allied Vision, Pike) are installed to acquire a bright-field image of the same sample. The DHT and bright-field imaging modes are switched using a flip mirror installed between DGM and L2. A program allowing for control of all of the mentioned 101 equipment is implemented in LabVIEW (National Instruments).

2.2. Sample preparation

103

104

106

108

110

112

113

114

115

116

A crown hair sample was collected from a Caucasian male. To prepare the hair sample for imaging, we first adhered it to a 1 mm-thick microscope slide using double-sided tape. The slide was then placed on a bright-field microscope. Using a flat bladed Exacto knife in our left hand, we held the hair sample steady at an angle almost parallel to the surface of the microscope slide. We positioned a light source above our left hand, angled towards the right, to allow light to pass through the sample into the microscope. With another flat bladed Exacto knife held vertically in our right hand, perpendicular to the microscope slide, we made a downward-chopping motion to slice the hair sample into lengths of 150-200 µm. The hair sample was placed in index matching oil with refractive index of 1.55 (Cargille Labs) to minimize the diffraction effect. Polystyrene microspheres (Polysciences, Inc.) of 20 µm diameter were immersed in the immersion oil (Cargille Labs) of the refractive index 1.57, sandwiched between two round coverslips (No. 1, 35 mm diameter), and imaged to determine the iteration number to alleviate the missing-cone problem. Custom-made sea urchin embryo slides were purchased from

120

122

124

126

129

131

132

136

140

142

144

146

150

151

152

154

156

157

159

161

Carolina Biological Supply Company. The undyed embryos in different development stages were fixed and mounted with Eukitt mounting medium (Electron Microscopy Sciences, 15320) between two round coverslips. Gold nanoparticles of 100-nm diameter were purchased from nanoComposix, Inc. To resuspend the settled nanoparticles, the bottle containing the colloid was vigorously shaken for about 30 seconds. A $10\,\mu\text{L}$ liquid drop of suspension was evenly spread on a No. 1, round coverslip of 35 mm diameter and dried in air. A drop of Eukitt was added onto the coverslip and covered with another round coverslip. The sample was used after about 2 hours. The refractive index of Eukitt in the SWIR range was measured using synthetic phase microscopy, and given as $n(\lambda) = 1.4736 + 1.4887 \times 10^{-4} \lambda^2 + 0.0068/\lambda^2$, where λ is the wavelength in μm .

2.3. Data acquisition

Using bright-field imaging, the sample regions were easily located. Once a sample region is found, the LED light source is turned off, and the flip mirror is moved out of the beam path, allowing the SWIR light to pass from the continuum laser and tunable filter through the galvanometer mirrors and sample, through the rest of the system. The DHT data is acquired in the 1100–1650 nm wavelength range at the 50 nm step size. For each wavelength, 400 projection images are acquired. The starting position of the mirror M1 on the motorized stage is adjusted so that the fringes in the field of view have strong and equal contrast at the wavelength of 1350 nm. Due to the effect of chromatic aberration, each wavelength has an optimal mirror position which results in the highest contrast. The optimal mirror positions are manually determined in a calibration experiment, where the mirror is translated along the optical axis until the image with highest interference fringe contrast is found for each wavelength. These mirror locations are recorded and then used by the LabVIEW program to automatically translate the mirror so that the interference fringes remain at the highest contrast as the wavelength is scanned. At each wavelength, the galvanometer scanner changes the angle of incidence, allowing us to capture 400 images of the sample at varying angles up to 40°. After acquiring the sample data set, another set of images is acquired after moving the sample out of the field of view. The background data set is acquired only once and used for all the sample data sets. The total data acquisition time to collect 12 wavelength stacks of 3D tomograms (400 images per each tomogram) is about 7 minutes for each sample and background data set.

2.4. Data processing

For each wavelength λ , a series of interferogram images is recorded while changing the illumination direction, $\overrightarrow{k_0}$. From each raw interferogram image, the amplitude and phase distributions of the light can be extracted using a standard fringe analysis technique[17]. Using Eqs. (1a) and (1b), we normalize the amplitude image for the sample with that of the background (i.e., the amplitude image recorded without the sample) and subtract the phase image for the background from that of the sample.

$$A(x,y;\lambda,\overrightarrow{k_0}) = A^{(s)}(x,y;\lambda,\overrightarrow{k_0})/A^{(b)}(x,y;\lambda,\overrightarrow{k_0}),$$
(1a)

$$\Phi(x,y;\lambda,\overrightarrow{k_0}) = \Phi^{(s)}(x,y;\lambda,\overrightarrow{k_0}) - \Phi^{(b)}(x,y;\lambda,\overrightarrow{k_0}).$$
 (1b)

Figure 2 shows examples of amplitude and phase images acquired with the system shown in Fig. 1. Figures 2(a) and 2(b) show the amplitude and phase images acquired at 1100 nm wavelength, respectively. Figures 2(c) and 2(d) show the amplitude and phase images acquired at 1500 nm wavelength, respectively. Figure 2(e) is a bright-field image of the same sample.

163

For each wavelength and illumination direction, a scattered light field, $U_s(x, y; \lambda, \overrightarrow{k_0})$, can be synthesized. With the first-order Born approximation[18], the scattered light field is synthesized using

$$U_s(x,y;\lambda,\overrightarrow{k_0}) = A(x,y;\lambda,\overrightarrow{k_0}) \exp\left[i\Phi(x,y;\lambda,\overrightarrow{k_0})\right] - 1.$$
 (2)

With the first-order Rytov approximation[19], the scattered light field is synthesized using

$$U_s(x, y; \lambda, \overrightarrow{k_0}) = \ln(A(x, y; \lambda, \overrightarrow{k_0})) + i\Phi(x, y; \lambda, \overrightarrow{k_0}). \tag{3}$$

The scattering potential F(X, Y, Z) can be defined for an imaged sample as a function of the absorption and refractive index properties.

$$F(X,Y,Z) = -(2\pi/\lambda)^2 ([n(X,Y,Z) + ik(X,Y,Z)]^2 - n_m^2), \tag{4}$$

where n_m is the refractive index of the medium in which the sample is immersed, n(X,Y,Z) is the 3D refractive index distribution in the sample, and k(X,Y,Z) is the 3D distribution of absorption constant, which can be related to the absorption coefficient $\mu(X,Y,Z)$ by $\mu(X,Y,Z) = (4\pi/\lambda)k(X,Y,Z)$.

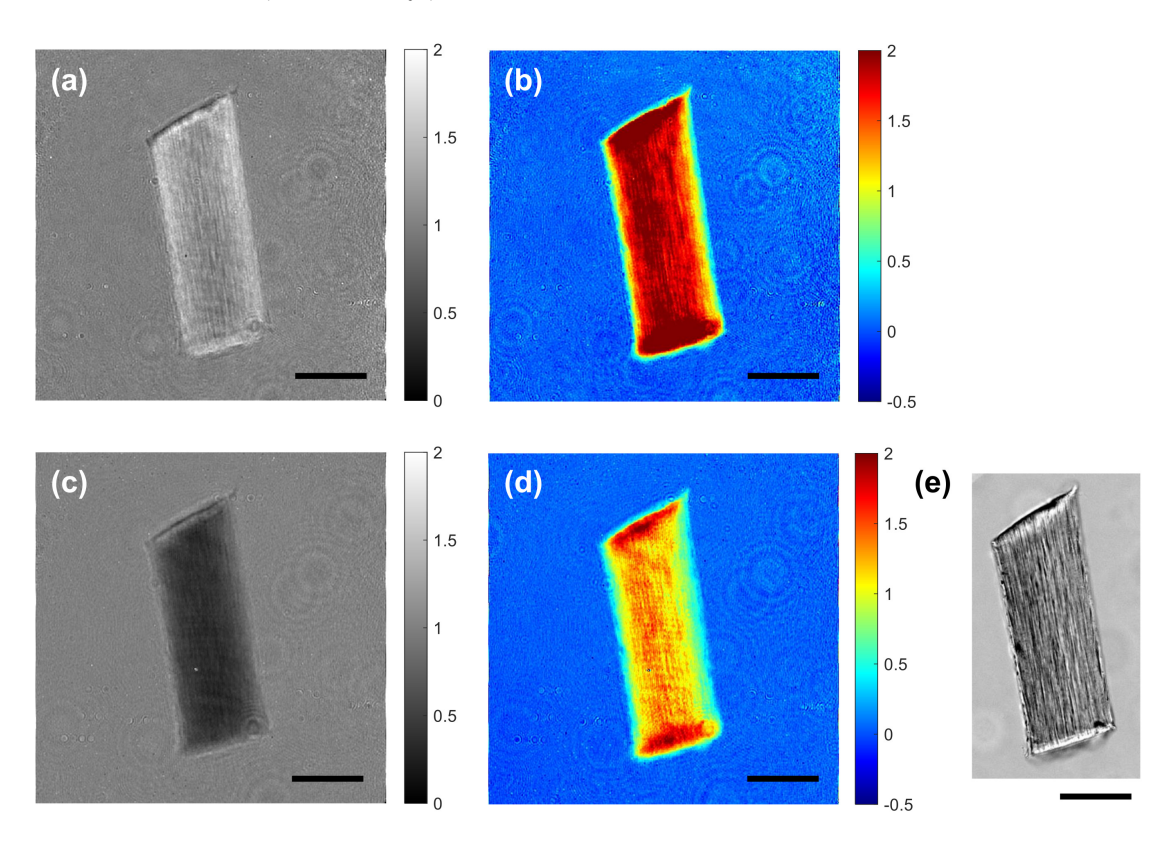


Figure 2. Example images acquired with the developed system. (a,b) show the amplitude and phase images of a hair, respectively, imaged at the wavelength of 1100 nm. (c,d) show the amplitude and phase images of the same hair, respectively, imaged at the wavelength of 1500 nm. The amplitude images in (a,c) are normalized with the background images, i.e., the amplitude images acquired without the sample at the corresponding wavelengths. The phase images in (b,d) are shown after subtracting the background images, i.e., the phase images acquired without the sample at the corresponding wavelengths (unit: radian). The amplitude and phase images for the two different wavelengths (1100 nm and 1500 nm) clearly show the wavelength-dependent absorption and refractive index properties of the hair. (e) shows a bright-field image of the same hair. Scale bars: 50 μm.

The scattered light fields given in Eqs. (3) and (4) can be related to the scattering potential of the imaged specimen, V(x, y, z), by Eq. (5)[20]. The first-order Born

approximation is valid when the size of the imaged object is very small, whereas the first-order Rytov approximation is valid when the refractive index increment is small at the boundaries. For hair samples, the first-order Rytov approximation is more appropriate, because the hair is thick, but its absorption constant k is only about 5×10^{-3} , which corresponds to the absorption coefficient μ of $400~cm^{-1}$ at the wavelength of 1500 nm. The measured absorption coefficient of the sea urchin embryos is also small; thus, the use of the first-order Rytov approximation can be justified. For gold nanoparticles, the refractive index of gold is very different from that of water or the mounting medium we used. Thus, using the first-order Born approximation is more appropriate.

$$\widetilde{U}_{s}(U,V;\lambda,\overrightarrow{k_{0}}) = \frac{\pi}{iw}\widetilde{F}(U-u_{0},V-v_{0},W-w_{0}), \tag{5}$$

where \tilde{U}_s and \tilde{F} are the 2D Fourier transform of U_s and the 3D Fourier transform of F, respectively, $W = \sqrt{(n_m/\lambda)^2 - U^2 - V^2}$, and (u_0, v_0, w_0) are the components of the wave vector $\overrightarrow{k_0}$ for the incident beam, which satisfy $u_0^2 + v_0^2 + w_0^2 = (n_m/\lambda)^2$. A graphical interpretation of Eq. (4) is to map the Fourier transform of the scattered field given in Eq. (2) or Eq. (3) to the spherical surface called the Ewald's sphere in the 3D spatial frequency space, as shown in Fig. 3.

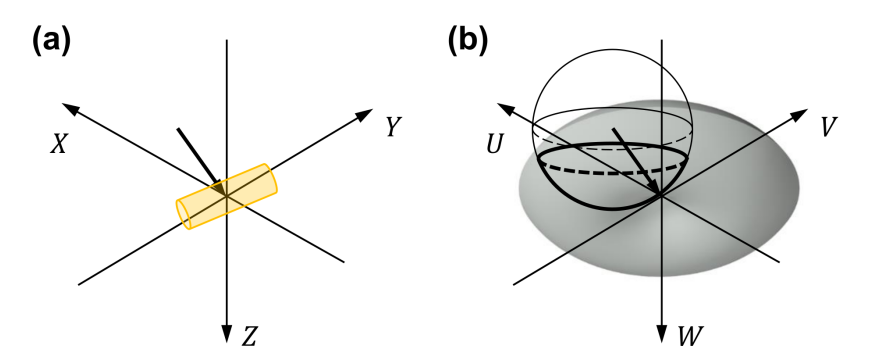


Figure 3. Digital holographic tomography data processing. For each wavelength, the amplitude and phase images recorded for an illumination angle are used to synthesize a scattered light field from the sample. The arrow in (a) represents the wave vector $\overrightarrow{k_0} = (u_o, v_0, w_0)$ of the illumination beam, whose magnitude and direction correspond to n_m/λ and the illumination direction onto the sample plane, respectively. As shown in (b), the Fourier transform of the scattered light field is mapped onto the Ewald's sphere, which is shifted in the opposite direction to the wave vector, in the 3D spatial frequency space. (X,Y,Z) are the Cartesian coordinates with Z being the optical axis direction. (U,V,W) are the spatial frequency components corresponding to (X,Y,Z), respectively.

The Ewald's sphere, onto which the scattered field is mapped, is shifted along different directions as the illumination angle is varied[18]. Thus, from the scattered fields measured for varying illumination angles, the 3D object spectrum (i.e., the components of $\tilde{F}(U,V,W)$) can be retrieved for many (U,V,W) values. After completing the mapping, we take the 3D inverse Fourier transform, which provides the scattering potential of the sample, and thus the 3D maps of refractive index and absorption constant (or absorption coefficient). Noteworthy, the refractive index of the reconstructed tomogram is underestimated due to the incomplete angular sampling, which is known as the missing-cone artefact[21]. The absorption coefficient can also be underestimated and even be negative due to the missing cone. For polystyrene microspheres, 300 iterations produced the mean refractive index value equal to that measured with a different method. The same iteration number is used for the reconstruction of the hair, which also has a circular cross section.

3. Results

3.1. 3D maps of absorption and refractive index of human hair

Figure 4 shows examples of the absorption coefficient and refractive index maps obtained from the DHT measurement. At the wavelength of 1100 nm, the absorption coefficient of the hair is very small, as shown in Fig. 4(a). The negative absorption coefficient is an artefact due to the missing cone, the coherent speckle, or both. Figure 4(b) shows that the refractive index of the hair is about 1.538 at the wavelength of 1100 nm. The high refractive index near the edges is an artefact, which is excluded in calculating the mean refractive index. As shown in Fig. 4(c), the absorption coefficient dramatically increases to about 400 cm^{-1} as the wavelength is increased to 1500 nm, while the refractive index decreases to about 1.534.

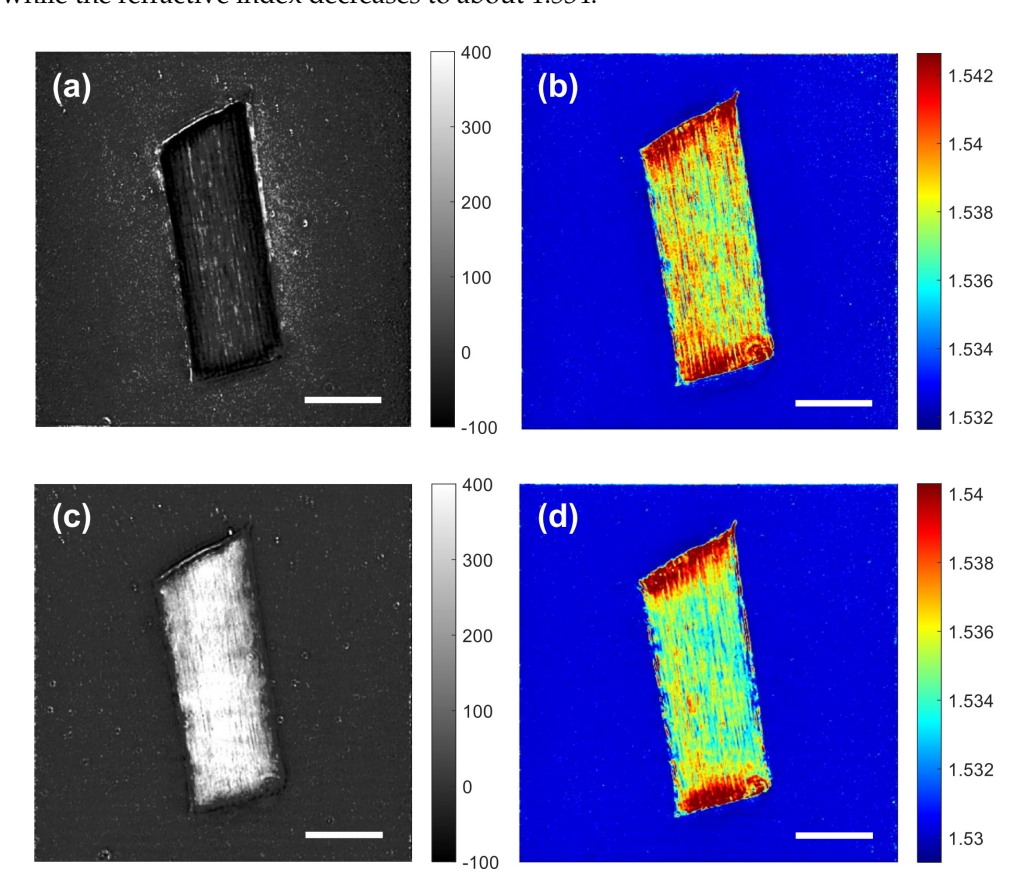


Figure 4. Examples of the absorption coefficient and refractive index maps reconstructed from a series of the scattered field measurements. (\mathbf{a} , \mathbf{b}) show the absorption coefficient and refractive index maps, respectively, for the center cross section at the wavelength of 1100 nm. (\mathbf{c} , \mathbf{d}) show the absorption coefficient and refractive index maps, respectively, for the center cross section at the wavelength of 1500 nm. The unit for the absorption coefficient is cm^{-1} . Scale bars: 50 μ m.

Figure 5(a) shows a 3D rendered image of the hair, which was calculated from the 3D refractive index map obtained at 1100 nm. Figure 5(b) shows vertical cross sections of the hair at 30 µm intervals, which are extracted from the 3D absorption coefficient map measured at the wavelength of 1500 nm. In the 3D absorption map at 1500 nm, we expect to see a combination of water bands as well as weak protein bands. Figures 5(c) and 5(d) show the mean absorption coefficient and the mean refractive index value, respectively, in the wavelength range of 1100–1650 nm. The shape of the measured absorption coefficient matches well with the absorbance profiles obtained with diffuse reflectance measurements[22–24]. We could not find the refractive index dispersion of hair in the literature. The refractive index of the hair shown in Fig. 5(d) can be fit to the Cauchy-Schott equation $n(\lambda) = 1.5305 + 1.3649 \times 10^{-4} \lambda^2 + 0.0089/\lambda^2$ with the RMSE

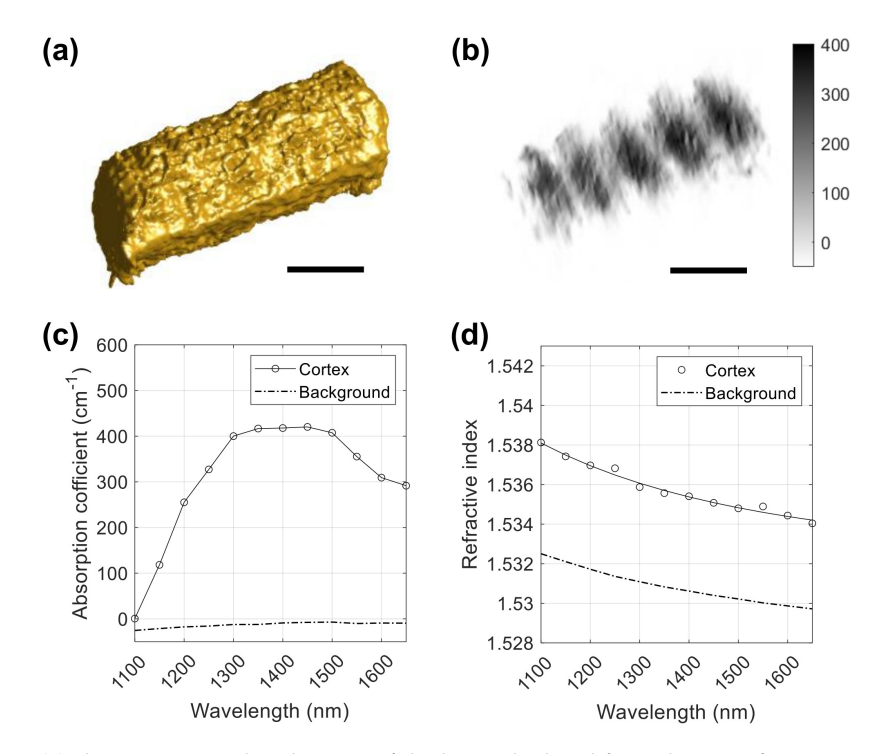


Figure 5. (a) shows a 3D rendered image of the hair calculated from the 3D refractive index map at the wavelength of 1100 nm. Although the optical system is capable of 5 nm spectral resolution, the step size of 50 nm was found to provide adequate spectral resolution to capture the relevant characteristics of the absorbance of the hair sample in the SWIR wavelength range. (b) shows an example of the 3D absorption coefficient map of the hair at the wavelength of 1500 nm. Five vertical cross sections at 30 μ m intervals are shown as an example. (c,d) show the mean absorption coefficient and the mean refractive index value, respectively, of the hair sample as a function of the wavelength in the 1100–1650 nm range. Scale bars in (a,b): 50 μ m.

227

229

230

232

234

235

236

237

238

239

243

245

247

249

251

25 2

25.3

of 2.0×10^{-4} . To the best of our knowledge, this is the first report of the absorption coefficient and the refractive index of human hair in the SWIR range. We note that human hairs strongly absorb the visible light; thus, the absorption coefficient of a human hair cannot be obtained using the visible-light DHT system, which was presented in our previous publication[1].

3.2. 3D refractive index imaging of sea urchin embryos in different development stages

We performed 3D refractive index imaging of the sea urchin embryos in different development stages: egg, 2 cells, 4 cells, morula, blastula, and gastrula stages. Figure 6 shows the horizontal cross section of each embryo at the wavelength of 1100 nm. For comparison, we have acquired bright-field images of the same samples, which are shown in Fig. 7. In Fig. 6, we can see that the embryos in the 2-cell and 4-cell stages have higher refractive index values than the other embryos in the egg, morula, blastula, and gastrula stages. The 2-cell and 4-cell embryos also have smaller sizes. Considering the refractive index is proportional to the density of non-aqueous content (i.e., dry mass) in a biological cell[25,26], Figs. 6 and 7 show that sea urchin embryos experience the change in mass density through a volume contraction and expansion. For a more quantitative analysis, we selected the intracellular region, whose refractive index value is higher than that of the background medium by at least 0.005. Figure 8 shows the distribution of the refractive index values in the selected region for each embryo. On each box, the central mark indicates the median, the bottom and top edges indicate the 25th and 75th percentiles, respectively, and the whiskers mark the range of the data points not considered outliers. Figure 8 indeed shows that the median refractive index of the 2-cell embryo was 1.505, which was 0.010 higher than that of the egg (1.495). The median refractive index of the 4-cell embryo was 1.500, which was 0.005 lower than that of the 2-cell embryo. The median refractive index was further decreased for the embryos in the later development stages. We note that the embryos used for the imaging were fixed with alcohol and mounted with Eukitt, which altered the refractive index values from their native values. Still, the change in the refractive index shown in Fig. 8 suggests a condensation of intracellular materials when the embryo progresses from the egg to the 2-cell stage, then a gradual decrease as the embryo develops further.

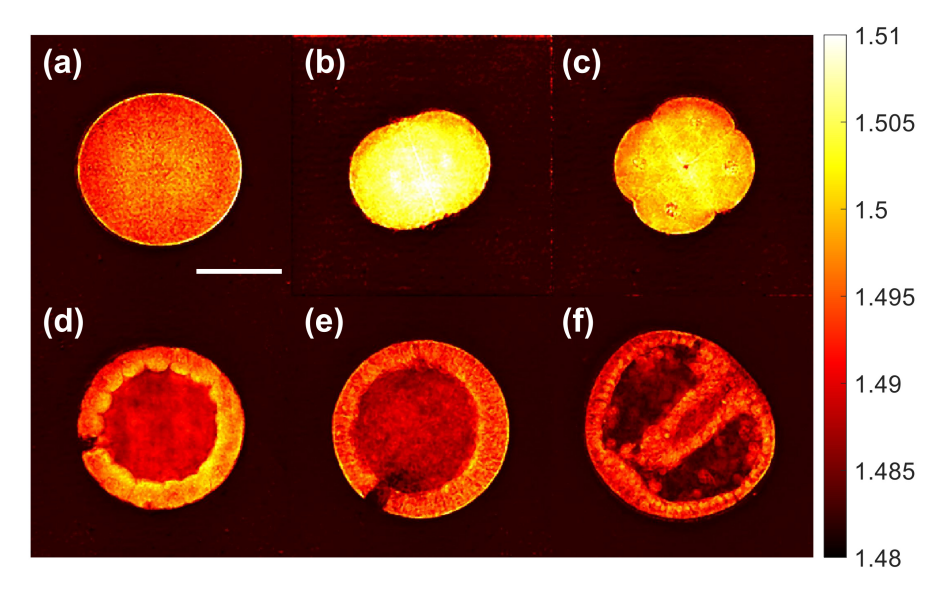


Figure 6. Refractive index cross sections of the sea urchin embryos in different development stages: (a) egg, (b) 2 cells, (c) 4 cells, (d) morula, (e) blastula, (f) gastrula. The refractive index was measured at the wavelength of 1100 nm. The scale bar $(50 \, \mu m)$ in (a) applies to all the images.

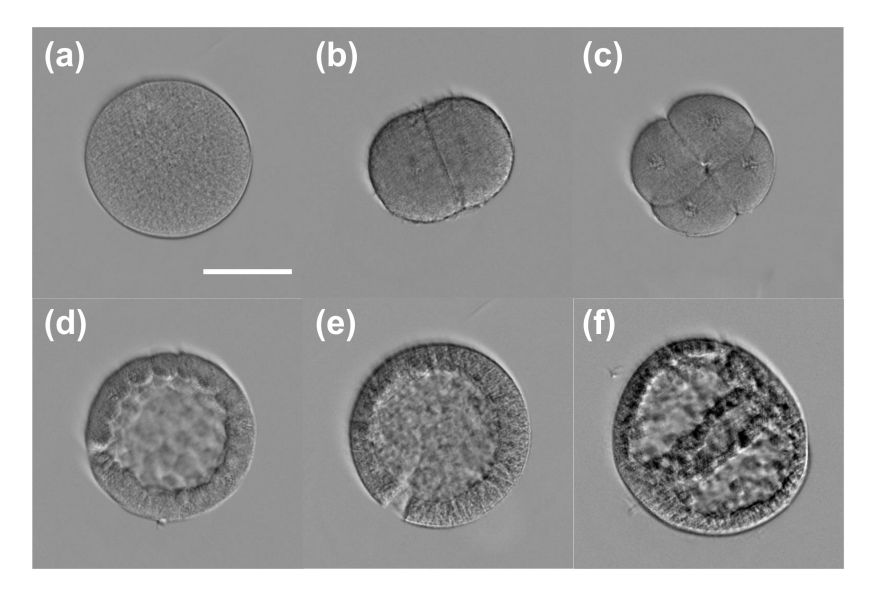


Figure 7. Bright-field images of the sea urchin embryos in different development stages: (a) egg, (b) 2 cells, (c) 4 cells, (d) morula, (e) blastula, (f) gastrula. The scale bar $(50 \, \mu m)$ in (a) applies to all the images.

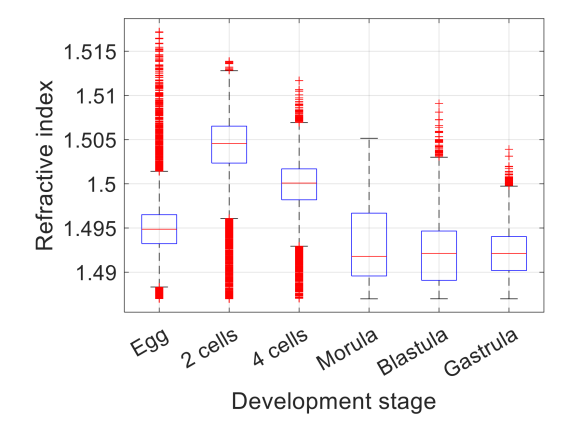


Figure 8. Refractive index of the sea urchin embryos in different development stages measured at the wavelength of 1100 nm. On each box, the central mark (red) indicates the median, the bottom and top edges (blue) indicate the 25th and 75th percentiles, respectively, and the whiskers (black) mark the range of the data points not considered outliers (red crosses).

257

259

261

263

265

267

268

269

270

272

274

276

277

278

3.3. 3D point spread function of SWIR digital holographic tomography system

We measured the 3D point spread function of the developed system using gold nanoparticles (GNPs) with the nominal diameter of 100 nm. In the raw interferogram images, we occasionally observed small dots of reduced intensity. Because the speckle noise could generate similar dots, we identified clusters of GNPs by looking for the dots that remained stationary as we scanned the illumination angle. Gold has a very different refractive index from water or Eukitt. For example, the refractive index of gold is 0.733 at 1100 nm. Due to the large refractive index difference between gold and the mounting medium, the absorption measurement is highly affected by the scattering. For the same reason, the refractive index value obtained with DHT becomes hard to interpret. To address these challenges, here we use the refractive index profile of GNPs only to assess the resolution. We also use the reconstruction algorithm based on the first-order Born approximation, which is more appropriate for small samples and less sensitive to the refractive index mismatch[27]. From the reconstructed 3D map, we obtained the horizontal (XY) and vertical (XZ) cross sections including the pixel with the highest value, which are shown in Figs. 9(a) and 9(b), respectively. The full width at half maximum (FWHM) values were used as measures of the transverse and axial resolution. The measured resolution was 1.43 µm (transverse) and 3.53 µm (axial) before applying the regularization. To image large samples, we sacrificed the spatial resolution. The current design of our DHT system is not diffraction limited, and the theoretical resolution is 1.44 µm, which matches well with the measured transverse resolution. Figures. 9(c) and 9(d) show the horizontal (XY) and vertical (XZ) cross sections of the 3D refractive index map after applying 30 iterations of the regularization. The resolution was measured to be $1.51 \, \mu m$ (transverse) and $1.57 \, \mu m$ (axial). The axial resolution was significantly improved, while the transverse resolution was lowered a little.

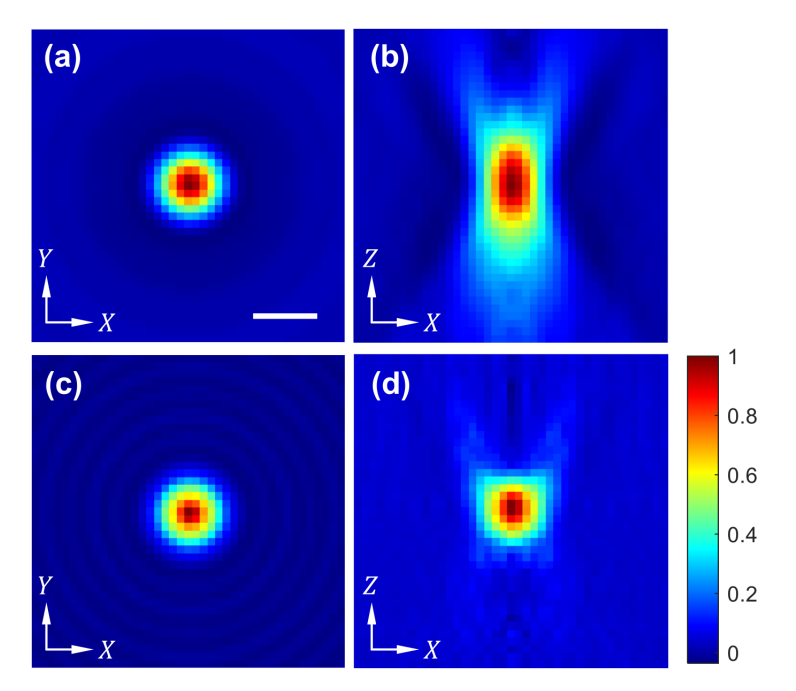


Figure 9. 3D point spread function (PSF) of the developed instrument measured with gold nanoparticles. (a) and (b) show the horizontal and vertical cross sections, respectively, of the 3D PSF before applying the regularization. (c) and (d) show the horizontal and vertical cross sections, respectively, of the 3D PSF after applying 30 iterations of the regularization. The 3D PSF measured with gold nanoparticles was averaged along the polar coordinate in each horizontal cross section. The transverse and axial resolutions determined with the full-width at half maximum (FWHM) are $1.43 \, \mu m$ and $3.53 \, \mu m$ before the regularization, and $1.51 \, \mu m$ and $1.57 \, \mu m$ after the regularization. The scale bar (2 μm) in (a) applies to all the images.

4. Discussion

Research on the optical properties of human hair has a wide range of practical applications in various fields, including cosmetic science[28], computer graphics[29], forensics[30], medicine[22], and anthropology[31]. In particular, the optical properties of hair in the SWIR range will allow for an accurate modeling of the light-skin interaction in the deep-tissue imaging using the SWIR light[32]. The information may also increase the accuracy of face recognition using the SWIR light, which is known to distinguish artificial hairs from natural ones[33].

The method demonstrated here will also be useful for a wide range of microscopic specimens showing the absorption or refractive index contrast in the SWIR range. For example, the developed system can be used to detect microplastics (e.g., polystyrene, polypropylene, polyethylene), which show distinct absorption and refractive index spectra in the SWIR range[34]. FTIR and Raman are the dominant methods, but they provide only the type, not the quantity (i.e., volume), of microplastic. In contrast, the DHT system can provide the quantity as well as the type of microplastic. Another potential application is to measure the optical properties of pharmaceutical powders in the SWIR range, which can provide an important input to the analysis of SWIR hyperspectral imaging used for the inline quality control of pharmaceutical products[35].

There are numerous research studies using DHT for live cell imaging[36]. The refractive index measurement in the SWIR range has an advantage in imaging thick specimens such as embryos. DHT in the visible range is typically applied to thin specimens, because the phase unwrapping often fails with a thick specimen. This problem can be alleviated in the SWIR range, because the phase alteration is inversely proportional to the wavelength; thus, an abrupt phase jump near the boundary is reduced.

The anisotropic resolution due to the missing cone is a well-known problem with beam-rotation DHT. Although the regularization improves the axial resolution and the accuracy of refractive index prediction, it should be used with caution, as the result depends on the types of constraints as well as various hyperparameters such as the number of iterations[37]. Combining the beam rotation with the sample rotation can provide nearly-isotropic resolution[14,15], although the data acquisition time will significantly increase.

5. Conclusion

We have demonstrated spectroscopic microtomography in the short-wave infrared range using digital holographic tomography and a wavelength-scanning laser. Applying the developed instrument to a human hair sample, we have measured the absorption coefficient and the refractive index in the wavelength range of 1100–1650 nm at the 50 nm step size allowing for structural and chemical imaging without the need for a special sample preparation. Further, we have measured the index of refraction of sea urchin embryos in six stages of development, showing condensation and expansion of intracellular materials. Using gold nanoparticles, the 3D point spread function was measured and the resolution was improved from 1.43 μ m (transverse) and 3.53 μ m (axial) to 1.51 μ m (transverse) and 1.57 μ m (axial) by using regularization.

Author Contributions: Conceptualization, C.J. and Y.S.; methodology, C.J., A.R.A., and Y.S.; analysis, C.J., A.R.A., P.S., and Y.S. All the authors have written the manuscript.

Funding: This research was funded by the National Science Foundation (1808331).

Conflicts of Interest: The authors declare no conflict of interest.

Abbreviations

The following abbreviations are used in this manuscript:

MIR Mid-infrared
NIR Near-infrared

SWIR Short-wave infrared

DHT Digital holographic tomography

TBPF Tunable bandpass filter
OPD Optical path difference
VOPL Variable optical path length
LED Light-emitting diode

References

1. Sung, Y. Spectroscopic microtomography in the visible wavelength range. *Phys. Rev. Appl.* **2018**, *10*, 054041.

- 2. Juntunen, C.; Abramczyk, A.R.; Woller, I.M.; Sung, Y. Hyperspectral three-dimensional absorption imaging using snapshot optical tomography. *Physical Review Applied* **2022**, *18*, 034055. Publisher: APS.
- 3. Martin, M.C.; Dabat-Blondeau, C.; Unger, M.; Sedlmair, J.; Parkinson, D.Y.; Bechtel, H.A.; Illman, B.; Castro, J.M.; Keiluweit, M.; Buschke, D.; Ogle, B.; Nasse, M.J.; J, H.C. 3D spectral imaging with synchrotron Fourier transform infrared spectromicrotomography. *Nat. Methods* **2013**, *10*, 861.
- 4. Bobroff, V.; Chen, H.H.; Delugin, M.; Javerzat, S.; Petibois, C. Quantitative IR microscopy and spectromics open the way to 3D digital pathology. *J. Biophotonics* **2017**, *10*, 598–606.
- 5. Dudak, J.; Zemlicka, J.; Karch, J.; Hermanova, Z.; Kvacek, J.; Krejci, F. Microtomography with photon counting detectors: improving the quality of tomographic reconstruction by voxel-space oversampling. *J. Instrum.* **2017**, *12*, C01060.
- Obst, M.; Wang, J.; Hitchcock, A.P. Soft X-ray spectro-tomography study of cyanobacterial biomineral nucleation. *Geobiology* 2009, 7, 577–591.
- 7. Sathyanarayana, D.N. Vibrational Spectroscopy: Theory and Applications; New Age International, 2015.
- 8. Griffiths, P.R.; De Haseth, J.A. Fourier transform infrared spectrometry; Vol. 171, John Wiley & Sons, Hoboken, 2007.
- 9. Ferraro, J.R. Introductory Raman Spectroscopy; Elsevier, 2003.
- 10. Ozaki, Y.; Huck, C.; Tsuchikawa, S.; Engelsen, S.B. Near-Infrared Spectroscopy: Theory, Spectral Analysis, Instrumentation, and Applications; Springer: Singapore, 2021.
- 11. Charriere, F.; Marian, A.; Montfort, F.; Kuehn, J.; Colomb, T.; Cuche, E.; Marquet, P.; Depeursinge, C. Cell refractive index tomography by digital holographic microscopy. *Opt. Lett.* **2006**, *31*, 178–180.
- 12. Lauer, V. New approach to Optical diffraction tomography yielding a vector equation of diffraction tomography and a novel tomographic microscope. *J. Microsc.* **2002**, 205, 165–176.
- 13. Choi, W.; Fang-Yen, C.; Badizadegan, K.; Oh, S.; Lue, N.; Dasari, R.R.; Feld, M.S. Tomographic phase microscopy. *Nat. Methods* **2007**. *4*. 717.
- 14. Vertu, S.; Flügge, J.; Delaunay, J.J.; Haeberlé, O. Improved and isotropic resolution in tomographic diffractive microscopy combining sample and illumination rotation. *Central European Journal of Physics* **2011**, *9*, 969–974. Publisher: Springer.
- 15. Simon, B.; Debailleul, M.; Houkal, M.; Ecoffet, C.; Bailleul, J.; Lambert, J.; Spangenberg, A.; Liu, H.; Soppera, O.; Haeberlé, O. Tomographic diffractive microscopy with isotropic resolution. *Optica* **2017**, *4*, 460–463. Publisher: Optica Publishing Group.
- 16. Haeberlé, O.; Belkebir, K.; Giovaninni, H.; Sentenac, A. Tomographic diffractive microscopy: basics, techniques and perspectives. *Journal of Modern Optics* **2010**, *57*, 686–699. Publisher: Taylor & Francis.
- 17. Creath, K. Phase-measurement interferometry techniques. *Prog. Optics* **1988**, *26*, 349–393.
- 18. Wolf, E. Three-dimensional structure determination of semi-transparent objects from holographic data. *Opt. Commun.* **1969**, 1, 153–156.
- 19. Devaney, A. Inverse-scattering theory within the Rytov approximation. Opt. Lett. 1981, 6, 374–376.
- 20. Sung, Y.; Choi, W.; Fang-Yen, C.; Badizadegan, K.; Dasari, R.R.; Feld, M.S. Optical diffraction tomography for high resolution live cell imaging. *Opt. Express* **2009**, *17*, 266–277.
- 21. Sung, Y.; Dasari, R.R. Deterministic regularization of three-dimensional Optical diffraction tomography. *J. Opt. Soc. Am. A* **2011**, 28, 1554–1561.
- 22. Zoccola, M.; Mossotti, R.; Innocenti, R.; Loria, D.I.; Rosso, S.; Zanetti, R. Near infrared spectroscopy as a tool for the determination of eumelanin in human hair. *Pigment cell research* **2004**, *17*, 379–385. Publisher: Wiley Online Library.
- 23. Miyamae, Y.; Yamakawa, Y.; Ozaki, Y. Evaluation of physical properties of human hair by diffuse reflectance near-infrared spectroscopy. *Applied spectroscopy* **2007**, *61*, 212–217. Publisher: Society for Applied Spectroscopy.
- 24. Egawa, M.; Hagihara, M.; Yanai, M. Near-infrared imaging of water in human hair. *Skin Research and Technology* **2013**, *19*, 35–41. Publisher: Wiley Online Library.
- 25. Barer, R.; Tkaczyk, S. Refractive index of concentrated protein solutions. *Nature* 1954, 173, 821–822.
- 26. Sung, Y.; Tzur, A.; Oh, S.; Choi, W.; Li, V.; Dasari, R.R.; Yaqoob, Z.; Kirschner, M.W. Size homeostasis in adherent cells studied by synthetic phase microscopy. *Proceedings of the National Academy of Sciences* **2013**, *110*, 16687–16692.
- 27. Born, M.; Wolf, E. *Principles of Optics*; Cambridge University Press, 2019.
- 28. Hadjur, C.; Daty, G.; Madry, G.; Corcuff, P. Cosmetic assessment of the human hair by confocal microscopy. *Scanning: The Journal of Scanning Microscopies* **2002**, 24, 59–64.

- 29. Ward, K.; Bertails, F.; Kim, T.Y.; Marschner, S.R.; Cani, M.P.; Lin, M.C. A survey on hair modeling: Styling, simulation, and rendering. *IEEE transactions on visualization and computer graphics* **2007**, *13*, 213–234.
- 30. Brandes, S. Near-infrared spectroscopic studies of human scalp hair in a forensic context. PhD thesis, Queensland University of Technology, 2009.
- 31. Lasisi, T.; Ito, S.; Wakamatsu, K.; Shaw, C.N. Quantifying variation in human scalp hair fiber shape and pigmentation. *American journal of physical anthropology* **2016**, *160*, 341–352.
- 32. Smith, A.M.; Mancini, M.C.; Nie, S. Second window for in vivo imaging. Nature nanotechnology 2009, 4, 710–711.
- 33. Bhowmik, M.K.; Saha, K.; Majumder, S.; Majumder, G.; Saha, A.; Sarma, A.N.; Bhattacharjee, D.; Basu, D.K.; Nasipuri, M. Thermal infrared face recognition—a biometric identification technique for robust security system. *Reviews, refinements and new ideas in face recognition* **2011**, *7*, 113–138.
- 34. Serranti, S.; Fiore, L.; Bonifazi, G.; Takeshima, A.; Takeuchi, H.; Kashiwada, S. Microplastics characterization by hyperspectral imaging in the SWIR range. SPIE Future Sensing Technologies. SPIE, 2019, Vol. 11197, pp. 134–140.
- 35. Lyon, R.C.; Lester, D.S.; Lewis, E.N.; Lee, E.; Yu, L.X.; Jefferson, E.H.; Hussain, A.S. Near-infrared spectral imaging for quality assurance of pharmaceutical products: analysis of tablets to assess powder blend homogeneity. *Aaps Pharmscitech* **2002**, *3*, 1–15.
- 36. Popescu, G. Quantitative phase imaging of cells and tissues; McGraw-Hill Education, 2011.
- 37. Bertero, M.; Boccacci, P.; De Mol, C. Introduction to Inverse Problems in Imaging; CRC press, 2021.